REVIEW

Check for updates

Recent advances in the O-doped polycyclic aromatic hydrocarbons

Yangguang Xiang,†[a] Tong Zou,†[b] Kun Yang,[b] Jinling Li,*[a] Ya Zou [iD] *[c] and Zebing Zeng [iD] *[b]

The strategic heteroatom doping of polycyclic aromatic hydrocarbons (PAHs) has emerged as a powerful paradigm for engineering advanced organic materials with tailored optoelectronic function-alities. Compared to those incorporated with other heteroatoms, the oxygen (O)-doped PAH systems have received comparatively less attention. This review highlights the recent advances in the synthesis, optoelectronic properties, and organic electronic applications of representative O-doped PAHs, mainly focusing on pyranopyranyl-bridged analogues of anthanthrene, O-embedded quinoidal acenes, and furanyl-bridged fused benzofuranyl derivatives. By summarizing their optoelectronic properties and structure−property relationships, we hope this review might provide valuable insights into the further design of high-performance functional O-doped conjugated materials for organic electronics.

1. Introduction

Since the groundbreaking discovery of single-layer graphene,[1] π-conjugated polycyclic aromatic hydrocarbons (PAHs) as a type of model compounds for graphene or graphene nanoribbons (GNRs) have attracted considerable attention in both academic and industrial fields.[2] Due to their finite molecular sizes and atomically precise topologies, these materials exhibited open

band gaps together with tunable optical, electronic and mag-netic properties, making them particularly appealing for var-ious optoelectronic applications.[3] As a result, a large body of structurally diverse PAHs with tailored physicochemical proper-ties and optoelectronic characteristics have been developed over the past two decades. These materials have been exten-sively investigated as active layers in organic photovoltaics (OPVs),[4] organic field-effect transistors (OFETs)[5] and emissive layers in organic light-emitting diodes (OLEDs),[6] fluorescent probes in bioimaging,[7] and so on.

One of the most effective strategies to enrich the structural diversity and modulate the optoelectronic properties of PAHs is the incorporation of main-group elements or heteroatoms into their conjugated frameworks.[8] The introduction of these heteroatoms enables precise tuning of electronic structures

[a] *Department of Advanced Interdisciplinary Science and Technology, Technology University of Henan, Zhengzhou, 450001, China. E-mail: jinling_li@haut.edu.cn*

[b] *Department of Chemistry and Chemical Engineering, University of Hunan, Changsha, 410082, China. E-mail: zbzeng@hnu.edu.cn*

[c] *Department of Chemistry, National University of Singapore, 3 Science Drive 3, Singapore, 117543, Singapore. E-mail: e0147032@u.nus.edu*

† These authors contributed equally to this work

Yangguang Xiang received his BSc degree in 2021 from Huaibei Normal University. Now, he is a master student at the College of Advanced Interdisciplinary Science and Technology, Henan University of Technology. His research pro-jects focus on synthetic metho-dology.

Yangguang Xiang

Tong Zou received her BE degree in 2024 from Nanchang Hangkong University. Now, she is a master student at the College of Chemistry and Chemical Engineering, Hunan University. Her research projects focus on organic conjugated radi-cals and device application.

Tong Zou

This journal is © The Royal Society of Chemistry 2025

J. Mater. Chem. C, 2025, **13**, 14187–14201 | **14187**

through orbital hybridization and electron density redistribution, thereby modulating photophysical features, redox properties, and so on.[9] On the other hand, heteroatoms can influence the intermolecular self-assembly behaviours of PAH molecules through extra heteroatom-mediated noncovalent interactions, offering great possibility to enhance intermolecular orbital overlap, reduce energetic disorder, and improve charge transport characteristics.[10]

In contrast to heteroatom doping with elements such as boron (B),[11] nitrogen (N),[12] phosphorus (P),[13] or sulfur (S),[14] the oxygen (O)-doped PAH systems have received comparatively less attention.[15] However, it has been reported that the doping of oxygen (O) atoms has been shown to effectively tune the molecular orbital configurations of the resulting PAHs, and stabilizing their high-lying HOMOs (highest occupied molecular orbital) and suppressing the high chemical reactivity of many electron-rich polycyclic π-conjugated systems.[16] Notably, compared to sulfur atoms, which have similar electron configurations, oxygen atoms possess a smaller atomic radius (1.21 Å vs. 1.85 Å) and higher electronegativity (3.44 vs. 2.58) to form strong O-mediated hydrogen bonding interactions, thus might trigger a strong intramolecular charge push–pull effect and promote close intermolecular packing, both of which are beneficial for achieving high-performance organic electronic materials.[17] With the increasing number of reported O-doped PAHs and recent advances in the field, a systematic review of their design principles and structure–property relationships is urgently needed to provide insight for the further development and property improvement of these materials. Therefore, in this review we will summarize recent progress in O-doped PAHs, mainly focusing on three representative classes of materials: (1) pyranopyranyl-bridged analogues of anthanthrene, (2) O-doped quinoidal acenes, and (3) furanyl-bridged fused benzofuran. Their synthesis, optoelectronic properties, and applications in organic electronics will be discussed and analysed, for the purpose of providing valuable insights into the organic electronic material community.

2. Pyranopyranyl-bridged O-doped PAHs

2.1 O-Doped anthanthrene analogues

In the naphthalene molecule, the carbon atoms at the 1 and 8 positions are the so-called *peri* positions, where substituents are unusually close compared to other positions. This spatial closeness contributes to the unique chemical and physical properties of the naphthalene derivatives.[18] *Peri*-Xanthenoxanthene (**PXX**), described as the O-doped anthanthrene analogue, has been known for nearly a century. Its first synthesis was reported in 1926 by Pummerer and co-workers, who obtained the yellow crystalline solid *via* a copper-mediated cyclization of [1,1′-binaphthalene]-2,2′-diol (Fig. 1a).[19] With the growing interest in organic molecules exhibiting conductive properties, **PXX** has recently garnered renewed attention, particularly for its role in conductive charge transfer complexes.[20] This resurgence underscores the evolving significance of **PXX** as a key structural motif in the design of next-generation functional materials. Compared to anthanthrene, the substitution of certain carbon atoms with oxygen atoms in **PXX** lowers the reactivity of conjugated framework, thereby enhancing their chemical stability.[21] **PXX** exhibits an essentially planar molecular structure and typically adopts a one-dimensional (1D) face to face stacking arrangement in the solid state. This packing configuration is anticipated to promote strong intermolecular electronic coupling and efficient charge carrier transport.

Jinling Li

Dr Jinling Li received her BS degree from Soochow University in 2007 and PhD degree from National University of Singapore in 2012. Later, she joined Henan University of Technology. Her research work includes organic material synthesis and synthetic methodology.

Ya Zou

Dr Ya Zou received his BS degree from Hunan Agricultural University in 2013 and his master's degree from Hunan University in 2016. He then obtained his PhD degree from National University of Singapore in 2021. His research interests focus on the synthesis of extended π-electron systems with novel structures, organic diradicaloids, and functional materials for organic electronics.

Zebing Zeng

Prof. Zebing Zeng received his BS degree from Hunan University of Technology in 2004, a master's degree from Nankai University in 2007, and a PhD degree in Material Chemistry from National University of Singapore in 2012. As a full professor in Hunan University since 2014, his research focus on novel π-conjugated functional materials with unique optoelectronic, magnetic, and spin properties.
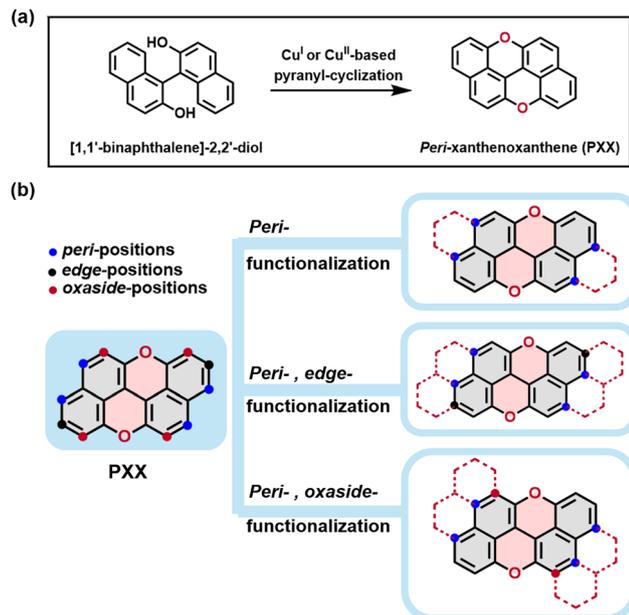
14188 | *J. Mater. Chem. C*, 2025, **13**, 14187–14201

This journal is © The Royal Society of Chemistry 2025

Fig. 1 General synthetic route to **PXX** (a) and representative synthetic strategies for the preparation of its derivatives (b).

Fig. 2 (a) Synthetic route to **2.1**. (b) UV–vis spectra of the 1,2,4-trichlorobenzene solution of **2.1** under air–bubbling. All curves were overlapped. (c) Transfer characteristics of the **2.1** TFT. Reproduced from ref. 23. Copyright 2009 American Chemical Society.

PXX serves as a fundamental building block for constructing O-doped PAHs and plays a pivotal role in the development of integrated optoelectronic devices. In recent years, diverse synthetic tactics have been developed to modify the **PXX** core, including peripheral functionalization with electron-withdrawing or electron-donating substituents, as well as extending the π-conjugated system. As illustrated in Fig. 1b, three main approaches have been developed for modifying the **PXX** framework through its *peri* positions: *peri*-functionalization alone, *peri–edge* functionalization and *peri-oxaside* functionalization. These distinct modification modes significantly influence the molecular stacking, consequently, have a profound impact on the charge transport properties of the resulting materials.[22]

Recent advances in *peri*-functionalization strategies have enabled precise control over π-conjugation and molecular packing, thus providing promising pathways toward high-performance optoelectronic materials. In 2009, Kobayashi *et al.* investigated the potential of 3,9-diphenyl-*peri*-xanthenoxanthene (**Ph-PXX, 2.1**), synthesized *via peri*-functionalization of the **PXX** core (Fig. 2a),[23] and explored its applications in organic thin-film transistors (OTFTs). **Ph-PXX** was synthesized *via* a Suzuki–Miyaura coupling reaction between 3,9-dibromo-*peri*-xanthenoxanthene (**Br-PXX, 2.2**) and phenyl boronic acid pinacol ester. The resulting compound **2.1** (**Ph-PXX**) adopted a 1D face-to-face stacking configuration and exhibited a high apparent electron mobility exceeding 0.4 cm^2 V^{-1} s^{-1} (Fig. 2c). It functioned as a p-type (hole-transporting) semiconductor material and maintained stable mobility even after five months under ambient conditions. Photostability test results demonstrated that the spectral profiles of **Ph-PXX** showed negligible changes after five days (Fig. 2b), indicating stable internal electronic transitions. These favorable properties were attributed to the introduction of oxygen atoms at the reactive
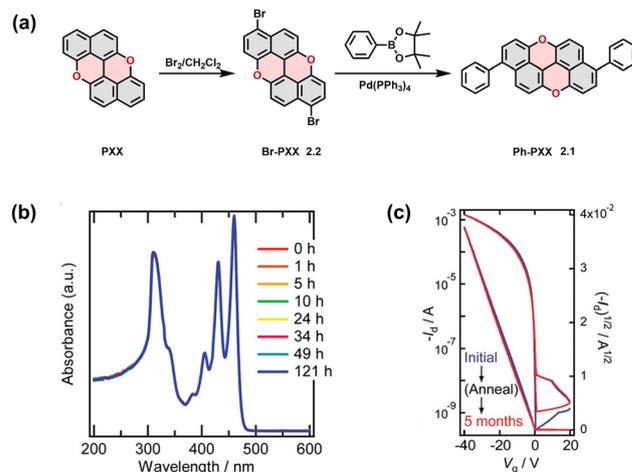
sites of anthanthrene core, which stabilizes the extended π-system and enhances charge injection efficiency in optoelectronic devices.

To further elucidate the effects of phenyl substitution and oxygen doping on stability and charge transport properties, Wang *et al.* conducted a comprehensive quantum chemical analysis.[24] Theoretical studies predicted that the introduction of oxygen atoms and phenyl groups at the reactive sites of the π-conjugated framework significantly improves the air stability of **Ph-PXX**. Oxygen doping preserves molecular planarity with minimal disruption to the π-conjugation. Interestingly, phenyl substitution at the **PXX** core induces a pronounced shift in charge transport behaviour from p-type to n-type (electron-transporting) semiconductor. These findings underscore the effectiveness of simple molecular modifications in tuning electronic properties and provide valuable insights for the rational *peri*-functionalization design of organic semiconductors.

In 2013, Qiu *et al.* developed a straightforward and efficient synthetic route to 1,7-dioctyl-*peri*-xanthenoxanthene (**3.1**) (Fig. 3a).[25] The synthesis began with 7-bromo-2-naphthol (**3.2**), proceeded through a sequence of FeCl$_3$-mediated oxidative coupling, hydroxy protection, Stille coupling, deprotection, and final O-cyclization facilitated by Cu(OAc)$_2$. In addition, they also synthesized two structural similar alkylated **PXX** derivatives using the same synthetic procedure as **3.1**, 2,8-dioctyl-*peri*-xanthenoxanthene (**2,8-DOPXX**) and 5,11-dioctyl-*peri*-xanthenoxanthene (**5,11-DOPXX**). The highly planar backbone of **3.1** facilitated a one-dimensional slipped face-to-face packing as evidenced by X-ray crystal structures (Fig. 3b). Spin-coated thin-film transistors based on compound **3.1** exhibited a hole transport capacity of 0.5 cm^2 V^{-1} s^{-1} and a high on/off ratio of 3.9 × 10^6 (Fig. 3c). The results demonstrated that the substitution sites of alkyl chain markedly influenced the molecular solid state packing arrangements and molecular packing distance (from 2.83 Å to 3.4 Å),
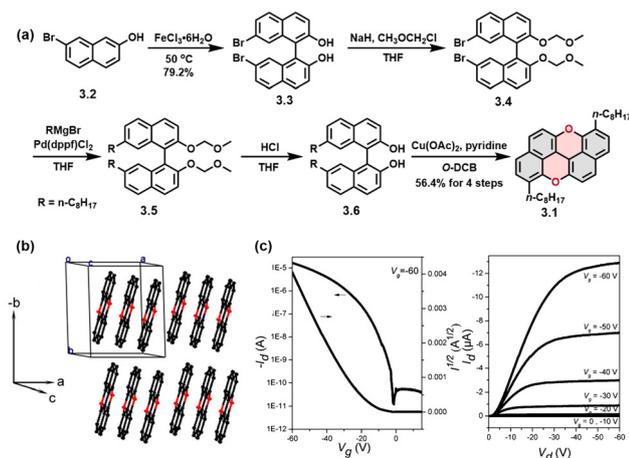
This journal is © The Royal Society of Chemistry 2025

J. Mater. Chem. C, 2025, **13**, 14187–14201 | **14189**

Fig. 3 (a) Synthetic route to **3.1**. (b) Crystal structures of **3.1**. (c) Field-effect transistors (FETs) characteristics of **3.1** transfer (left) plot and output (right) plot. Reproduced from ref. 25. Copyright 2013 American Chemical Society.

thereby significantly affecting their hole mobility from 0.04 cm^2 V^{-1} s^{-1} to 0.5 cm^2 V^{-1} s^{-1}.

In 2018, Wang's group reported a cost-effective **PXX**-centered small molecule, N^3,N^3,N^9,N^9-tetrakis(4-methoxyphenyl) xantheno-[2,1,9,8-*klmna*]xanthene-3,9-diamine (**4.1**), shown in Fig. 4a. They demonstrated its utility as a hole-transporting material in perovskite solar cells (PSCs).[26] Compound **4.1** was synthesized from **Br-PXX** (**2.2**) *via* a two-fold Buchwald–Hartwig cross-coupling reaction with 4,4′-dimethoxydiphenylamine. X-ray crystallography showed that **4.1** forms a 1D π-stacked columnar architecture along *a* axis, further assembled into a 3D framework through extensive C–H···O and C–H···π interactions (Fig. 4b). When
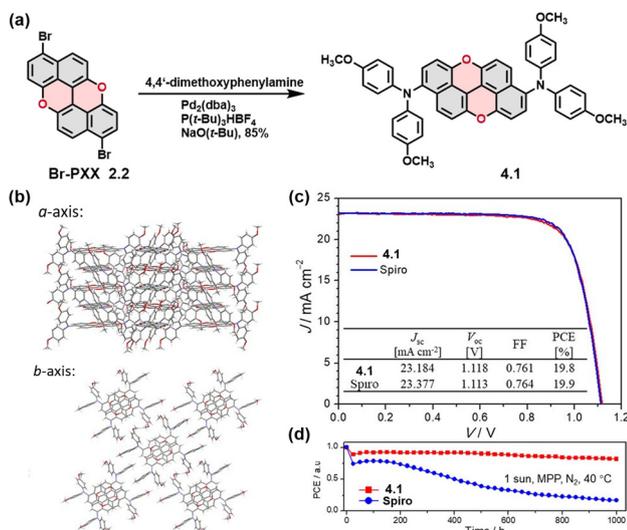

Fig. 4 (a) Synthetic route of **4.1**. (b) Crystal structures of **4.1** along *a*-axis view (top) and *b*-axis view (bottom). (c) *J–V* characteristic of a PSC with **4.1** and spiro. (d) Evolution of normalized PCEs of un-encapsulated devices at 40 °C under nitrogen. Reproduced from ref. 26. Copyright 2019 Wiley-VCH Verlag GmbH & Co. KGaA, Weinheim.

employed as the hole-transporting layer in PSCs, thin films of **4.1** achieved an impressive power conversion efficiency (PCE) of 19.8% under standard AM 1.5G conditions, comparable to that of the state-of-the-art spiro (PCE of 19.9%) (Fig. 4c). Remarkably, under continuous one sun illumination at 40 °C for 1000 hours, the devices incorporating **4.1** maintained over 80% of their initial efficiency, in sharp contrast to spiro based devices that retained only 17% (Fig. 4d). These results highlighted the excellent long-term operational stability and potential of *peri*-functionalized **PXX**-derived materials for next-generation photovoltaic applications.

To enrich the internal structure of **PXX**, Bonifazi and colleagues have recently conducted pioneering research on π-conjugation extension at the *peri*-positions, *oxaside*-positions, and *edge*-positions of the **PXX** core. They successfully synthesized a series of π-extended **PXX** derivatives, featuring diverse ribbon-like architectures with armchair or zigzag peripheries (Fig. 5), mainly accomplished through a modified Pummerer *O*-annulation reaction. In 2016, Bonifazi *et al.* reported a novel synthetic approach toward two unprecedented O-doped armchair-edged nanoribbons, namely bispyranopyran (**5.1**) and tripyranopyran (**5.2**), featuring *peri*- and *oxaside*-functionalized **PXX** derivatives (Fig. 6a).[27] These structures were constructed *via* a stepwise planarization of oligonaphthalene precursors involving the critical intramolecular C–O bond formation by CuI-catalyzed ring closure reaction. The key intermediates, **5.3** and **5.5**, were subjected to intramolecular etherification as the first oxidative ring closure step. Subsequent demethylation with BBr$_3$ enabled a second ring closing reaction, affording the fully fused oxygen doped systems **5.1** and **5.2**, respectively. X-ray structure analysis revealed that **5.1** had a nearly planar boomerang-shaped framework with four oxygen atoms at its periphery (Fig. 6b). In the packing structure, **5.1** formed a well-ordered columnar stacking arrangement driven by strong face-to-face π–π stacking interactions (Fig. 6c). Unfortunately, no self-assembly behaviour was observed in the solid state of **5.2**.

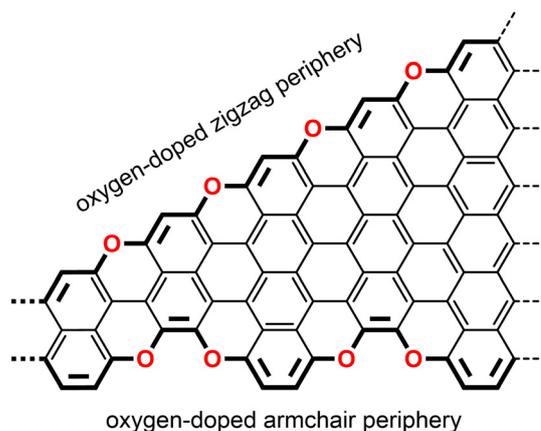In 2018, the same team achieved a significant milestone with the first synthesis of an O-doped zigzag-edged nanoribbon

Fig. 5 The representative armchair and zigzag edge structures of O-doped PAHs.

14190 | *J. Mater. Chem. C*, 2025, **13**, 14187–14201

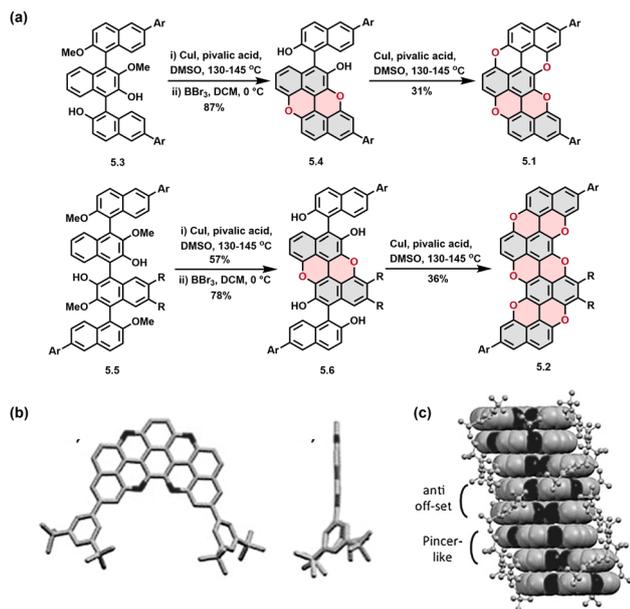This journal is © The Royal Society of Chemistry 2025

Fig. 6 (a) Synthetic routes to **5.1** and **5.2**. Ar = 3,5-di(*tert*-butyl) phenyl. (b) X-ray crystallographic structures of **5.1** (top view and side view). (c) Columnar π–π stacking of **5.1** in solid state (3.3 Å). Reproduced from ref. 27. Copyright 2016 Wiley-VCH Verlag GmbH & Co. KGaA, Weinheim.
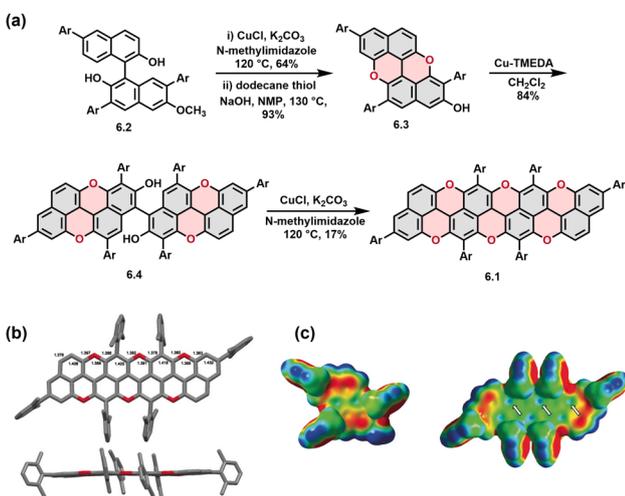

Fig. 7 (a) Synthetic routes to **6.1**. Ar = 2,6-dimethylphenyl. (b) X-ray crystal structures of **6.1**, top view (top) and side view (bottom). (c) Electrostatic surface potentials (ESP) calculations of **6.1**. Reproduced from ref. 28. Copyright 2018 Wiley-VCH Verlag GmbH & Co. KGaA, Weinheim.

(**6.1**, Fig. 7a),[28] featuring π-extension at both the *peri-* and *edge*-positions of the **PXX** core. The synthetic strategy mirrored that of previously reported O-doped armchair-edged nanoribbons (**5.1** and **5.2**). The route involved a CuCl-catalysed C–O planarization of **6.2**, followed by demethylation to generate the hydroxylated intermediate **6.3**. Subsequent homodimerization in the presence of Cu-TMEDA (*N*,*N*,*N'*,*N'*-tetramethylethylenediamine) yielded the key intermediate **6.4**. A final oxidative C–O planarization under similar CuCl-catalyzed conditions afforded nanoribbon **6.1** as an orange solid. These nanoribbons exhibited

commendable chemical and thermal stability. X-ray crystallographic analysis of **6.1** revealed the absence of face-to-face π–π stacking interactions. Instead, the molecules adopted an edge arrangement by C–H⋯π interactions, likely due to the steric repulsion from the peripheral phenyl substituents (Fig. 7b). Notably, as the O-doped conjugated backbone extended from **6.3** to **6.1**, the optical band gap narrowed from 3.29 eV to 2.78 eV, accompanied by a shift in the HOMO energy level from −5.14 eV (**6.3**) to −4.74 eV (**6.1**). Additionally, the emission spectra of compound **6.1** displays a pronounced red shift of approximately 74 nm compared to **6.3**. Electrostatic potential calculations further revealed a weak positive charge accumulation at the central ring (indicated by a white arrow) (Fig. 7c), suggesting notable charge depletion on the two inner naphthalene subunits. Importantly, **6.1** exhibited excellent photostability and thermal stability in the solid state at room temperature. Overall, these studies identified **6.1** as a strong electron donor with favourable frontier orbital alignment and structural robustness, making it a promising candidate in p-type organic semiconductor.

To further investigate the effect of π-extension along the **PXX** skeleton, the synthesis of π-extended **PXX** derivatives (**7.1** and **7.2**) were reported by Bonifazi *et al.* in 2017, *via* the fusion of naphthalene moieties at the peripheral termini of the **PXX** core (Fig. 8).[29] The key synthetic transformation involved Cu-TMEDA-catalysed oxidative C–C bond formation. Specifically, precursor **7.3** cross-coupled with 2-naphthol to afford **7.4** in 26% yield, while its self-dimerization produced **7.5** in 71% yield. Both intermediates were subsequently subjected to a Pummerer-modified Cu-catalysed intramolecular etherification to afford the pyranopyranyl derivatives (**7.1** and **7.2**). Due to the strong tendency to aggregate, these compounds show limited solubility. Photophysical and electrochemical studies were conducted to assess the effect of π-extension. UV-vis absorption maxima for **PXX**, **7.1** and **7.2** were observed at 444 nm (ε = 17 300 M^{-1} cm^{-1}), 556 nm (36 300 M^{-1} cm^{-1}) and 639 nm (66 400 M^{-1} cm^{-1}), respectively. The results demonstrated pronounced redshifts upon π-extension and confirmed an enhanced π-conjugation. Correspondingly, the HOMO–LUMO (lowest unoccupied molecular orbital) energy gaps decreased with extended π-conjugation, primarily due to elevated HOMO energy levels (from −4.71 eV for **PXX** to −4.49 eV for **7.1** and −4.38 eV for **7.2**), indicating enhanced electron-donating properties (Fig. 8b). DFT calculations further supported this trend, revealing delocalization of HOMO/LUMO over the entire π-surface, with significant O-atom contributions to the HOMO in **7.1** and **7.2** (Fig. 8c). These results, corroborated by electrochemical characterization, indicated that O-cyclization strongly influenced the HOMO energy level. Collectively, oxygen-cyclization profoundly influenced optoelectronic properties of π-extended **PXX** derivatives.

In 2018, Bonifazi *et al.* expanded this approach by introducing electron-withdrawing imide functionalities at the *peri*-position of **PXX** core to modulate frontier molecular orbital energies.[30] The resulting derivatives included a diimide (**PXXDI**, **8.1**) and two monoimides (**PXXMI**, **8.2** and **8.3**), with their synthetic pathways shown in Fig. 9. Compound **8.1** was

This journal is © The Royal Society of Chemistry 2025

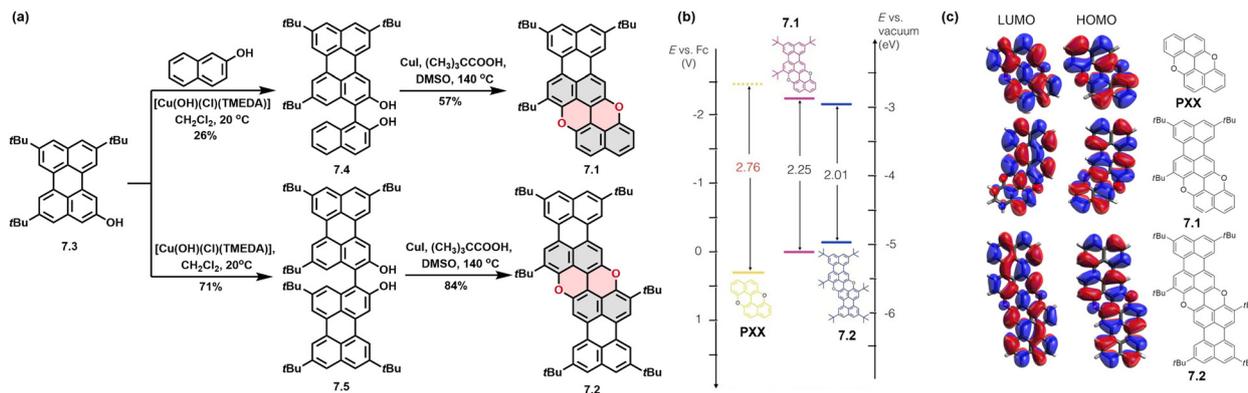*J. Mater. Chem. C*, 2025, **13**, 14187–14201 | **14191**

Fig. 8 (a) Synthetic routes to **7.1** and **7.2**. (b) Frontier orbital energies for compounds **PXX**, **7.1** and **7.2**. (c) Molecular orbitals **PXX**, **7.1** and **7.2**. Reproduced from ref. 29. Copyright 2016 Wiley-VCH Verlag GmbH & Co. KGaA, Weinheim.
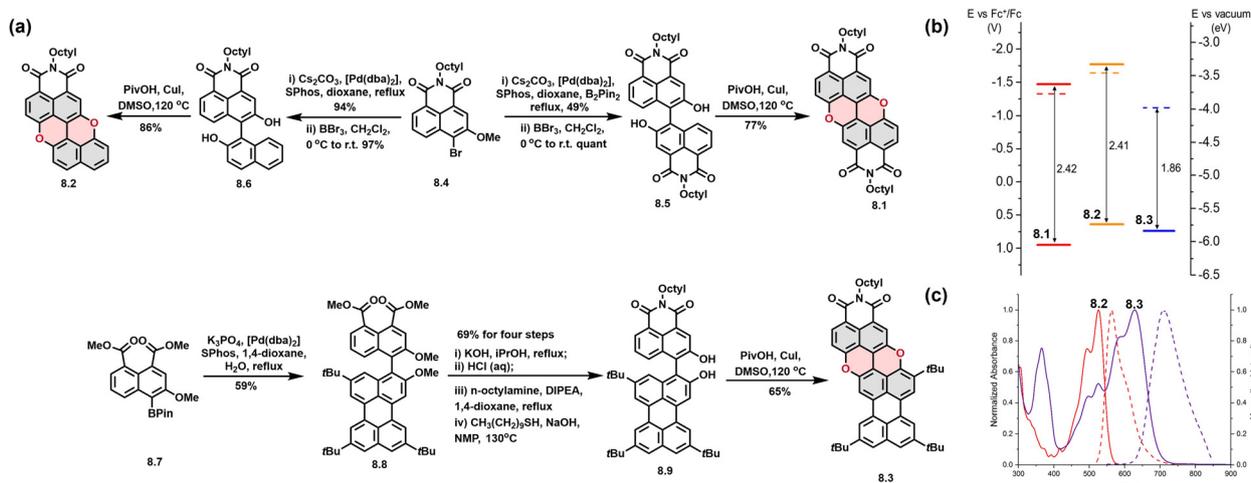

Fig. 9 (a) Synthetic routes to **8.1**, **8.2** and **8.3**. (b) Frontier orbital energies for **8.1**, **8.2** and **8.3**. (c) Absorption and emission spectra of **8.2** and **8.3**. Reproduced from ref. 30. Copyright 2018 American Chemical Society.

synthesized in a good yield (74%) from the bromo-substituted precursor **8.4**, through a four-step protocol, including Miyaura borylation, Suzuki cross-coupling, demethylation and Cu-facilitated oxidative etherification. A similar approach was employed for **8.2**. The synthesis of **8.3** required a more elaborate six-step route starting from **8.7**. First, **8.7** was subject to Suzuki cross-coupling with the relevant perylene bromide[31] to generate **8**, then processed through: (i) alkaline hydrolysis, (ii) acid-catalysed cyclization, (iii) imidization with n-octyl-amine, (iv) deprotection of the methoxy group, and finally, the key step of oxidative etherification to yield **8.3**. Photophysical studies revealed that imide functionalized **PXX** exhibited characteristic absorption maxima at 538 nm (ε = 43 500 M^{-1} cm^{-1} for **8.1**), 525 nm (ε = 17 800 M^{-1} cm^{-1} for **8.2**), and 628 nm (ε = 23 100 M^{-1} cm^{-1} for **8.3**). Given the existence of peri-fused naphthalene unit, **8.3** showed a marked red-shift compared to **8.2** (Fig. 9c). Cyclic voltammetry (CV) studies demonstrated that incorporating one imide group (**8.2**) or two (**8.1**) enhanced oxidative behaviour ($E_{red}^{1/2}$ = −1.77 eV for **8.2** and −1.47 eV for **8.1** vs. Fc$^+$/Fc in CH_2Cl_2), accompanied by reduced reductive

properties ($E_{ox}^{1/2}$ = 0.64 eV for **8.2** and 0.95 eV for **8.1**). Notably, **8.3** exhibited a significantly lowered LUMO level (Fig. 9b). These results underscored the strong electron-withdrawing effect of the imide functionality. Combined photophysical and redox analysis confirmed that imide insertion substantially modulated the excited state redox potential and frontier orbital energies of **PXX**-based systems.

In 2023, Zeng et al. developed a new molecular design strategy for synthesizing larger O-doped PAHs by incorporating oxygen atoms at the cove regions of naphthylamide frameworks, resulting in more extended π-systems than those of the typical **PXX** core.[32] As shown in Fig. 10a, the synthesis of **O-ADA** began with a Suzuki cross-coupling reaction between dimethoxy 1,5-dibromoanthracene and naphthalimide borate, affording intermediate **9.2** with a yield of 65%. Subsequently, **9.2** was oxidized with $FeCl_3$ to give compound **9.1**, which upon cyclization afforded the target product **O-ADA** in 25% yield. Compared to its oxygen-free analogue **ADA**, **O-ADA** featured both extended π-conjugation and a zigzag edge topology, the latter resulting from cove-region oxygen annulation (highlighted in

14192 | J. Mater. Chem. C, 2025, **13**, 14187–14201

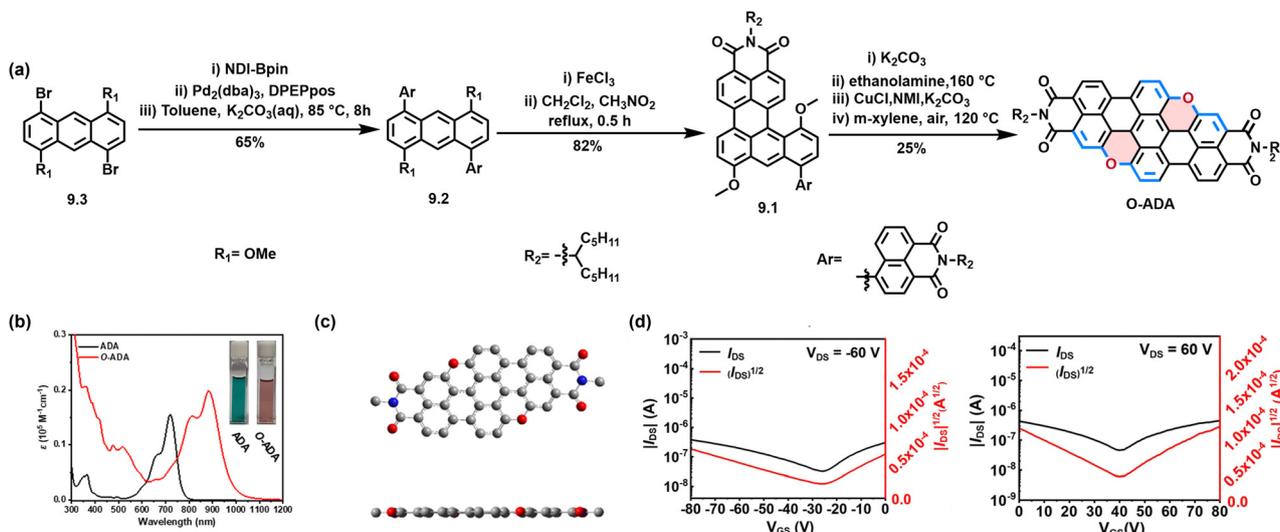This journal is © The Royal Society of Chemistry 2025

Fig. 10 (a) Synthesis routes to **O-ADA**. (b) UV-vis-NIR absorption spectra of **ADA** and **O-ADA**. (c) Optimized molecular geometries by DFT-calculation at the B3LYP/6-31G(d,p) level: front views and side views of **O-ADA**. (d) Transfer characteristics of **O-ADA**-based thin film OFET devices. Reproduced from ref. 32. Copyright 2023 The Royal Society of Chemistry.

blue in Fig. 10a). Density functional theory (DFT) calculations revealed that **O-ADA** adopted a highly planar geometry, in contrast to the distorted framework of **ADA**. It is attributable to the structural rigidity conferred by the *O*-annulation at the *cove* sites (Fig. 10c).

This structural modification also induced significant changes in optical properties. The UV-vis absorption spectrum showed that the maximum absorption wavelength of **O-ADA** was red-shifted by approximately 162 nm relative to **ADA**, corresponding to a narrowing of the optical band gap from 1.54 eV (**ADA**) to 1.12 eV (**O-ADA**), consistent with its more π-extension. Remarkably, in contrast to the n-type transport in **ADA**-based OFETs ($\mu_e = 3.2 \times 10^{-4}$ cm^2 V^{-1} s^{-1}), **O-ADA** devices exhibited a clear ambipolar characteristics with balanced hole and electron mobility of 1.07×10^{-3} cm^2 V^{-1} s^{-1} and 7.6×10^{-4} cm^2 V^{-1} s^{-1}, respectively. (Fig. 10d) The emergence of p-type transport property can be attributed to the elevated HOMO energy level from -5.02 eV for **O-ADA** to -5.29 eV for **ADA**, which facilitates hole injection. These results underscored the critical influence of oxygen annulation on molecular planarity, energy levels, and charge transport behaviour, offering valuable insights into the design of next-generation ambipolar semiconductors.

2.2 O-Doped quinoidal acenes

The incorporation of quinoidal units into PAHs has emerged as a powerful strategy for tuning electronic structures, enhancing π-electron delocalization, and introducing open-shell diradical character (Fig. 11).[33] In particular, embedding quinoidal moieties into O-doped acenes significantly strengthens electronic communication between the central quinoidal core and adjacent aromatic rings, also imparting distinctive electrochemical and photophysical properties, such as bandgap narrowing, redox behaviour, and spin activity, offering promising prospects for next-generation organic electronic and spintronic materials.
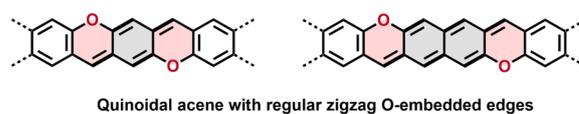

Quinoidal acene with regular zigzag O-embedded edges

Fig. 11 O-Doped quinoidal acenes with lateral areno-unit fused onto the central 1,4-benzoquinodimethane (left), 2,6-naphthoquinodimethane (right), *via* an oxygen linkage.

However, the extension of both the central quinoidal core and the lateral aromatic units can enhance diradical character, primarily due to the partial recovery of aromaticity in the quinoidal segment,[34] this also introduces molecular instability and poses significant synthetic challenges. Nonetheless, the strategy remains highly promising. Upon chemical oxidation, O-doped quinoidal acenes lose two electrons, forming isoelectronic species analogous to their all-carbon acene counterparts. As such, these charged derivatives serve as valuable model systems for probing the electronic properties of acenes.[35] Despite the difficulties associated with their synthesis, such as limited precursor availability, multi-step low-yield procedures, and the intrinsic instability of open-shell systems, remarkable advances have been made in recent year.

In 2009, Kalb and colleagues reported a low-cost synthesis and purification method for an O-doped quinoidal pentacene derivative (**10.1**), which serves as a viable material for p-type semiconductors in OFETs.[36] The key precursor **10.3** was synthesized from 1,4-bis-(1-ethoxyethoxy)benzene and subsequently treated with nitrobenzene to yield the O-doped pentacene **10.1** (Fig. 12a). XRD analysis revealed that **10.1** possesses a flat backbone and forms a slip-stacking pattern in the crystal structure (Fig. 12b). This ordered packing results in a low degree of structural disorder, enabling efficient charge transport. Consequently, single crystal OFETs based on **10.1** achieved hole mobilities as high as 0.16 cm^2 V^{-1} s^{-1}, whereas thin-film devices

This journal is © The Royal Society of Chemistry 2025

J. Mater. Chem. C, 2025, **13**, 14187–14201 | **14193**
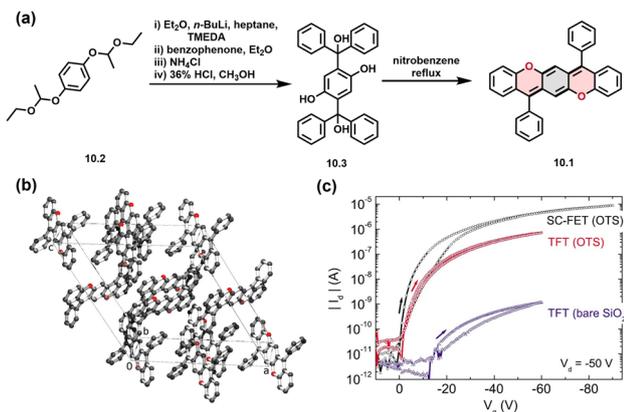
(a)

(b)

(c)

Fig. 12 (a) Synthetic routes to **10.1**. (b) Crystal structure of **10.1**. The molecules are ordered in slipped stacks along the crystallographic *b*-axis. (c) Transfer characteristic from a **10.1** single crystal FETs and thin-film transistor (TFT) with a bare SiO$_2$ gate dielectric. Reproduced from ref. 36. Copyright 2016 Wiley-VCH.

showed a reduced mobility of 0.01 cm^2 V^{-1} s^{-1} (Fig. 12c). Despite this drop, the thin-film transistors maintained desirable characteristics such as near-zero threshold voltage, low off-state current at 0 gate bias and small current hysteresis.

In 2019, Chen and collaborators discovered a practical and efficient synthetic strategy to access a bisphenalenyl-fused O-doped quinoidal radical cation **11(OTf)** (Fig. 13).[37] The synthesis began with lithiation of the dibromo compound **11.2**, followed by the nucleophilic addition to compound **11.1**. Subsequent dehydrogenation with 2,3-dichloro-5,6-dicyano-1,4-benzoquinone (DDQ) afforded the key intermediate **11.3**. Treatment of **11.3** with trifluoromethanesulfonic acid (TfOH) facilitated methyl ether deprotection and dual cyclization to yield the dicationic species **11.4**. Finally, reduction of **11.4** with sodium dithionite (Na$_2$S$_2$O$_4$) produced the ambient stable

(a)

(b)

(c)

(d)

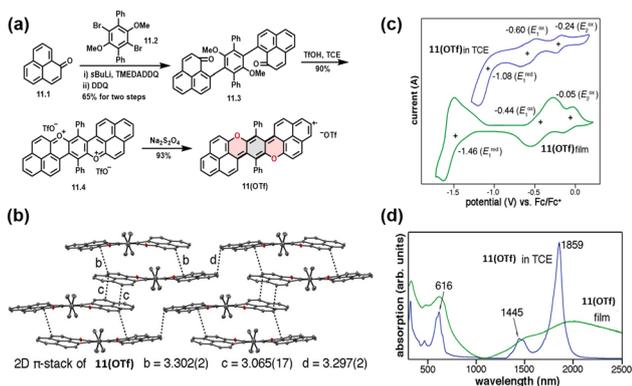**Fig. 13** (a) Synthetic routes to **11(OTf)**. (b) Solid-state π-assemblies of **11(OTf)** determined by single crystal XRD: (b) head-to-tail π-stacking, (c) head-to-head π-stacking, (d) tail-to-tail π-stacking. Interatomic distances are shown in angstroms (Å). (c) Cyclic voltammograms of **11(OTf)** in 1,1,2,2-tetrachloroethane (TCE) solution (0.1 mM, blue) and thin film on the electrode (green). (d) UV-vis-NIR absorption spectra of **11(OTf)** in solution and drop cast films. Reproduced from ref. 37. Copyright 2019 American Chemical Society.

radical cation **11(OTf)**. Optical characterization of **11(OTf)** in solution revealed prominent absorption maxima at 616 nm in visible, and at 1445 nm and 1859 nm in the Near Infrared (NIR). These absorption bands exhibited red-shifts and broadening in films (Fig. 13d), suggesting the presence of long-range π-conjugation enabled by intermolecular covalent-bonding interactions. Cyclic voltammetric electrochemical tests showed that the redox potential of **11(OTf)** in the solid state was greater than in solution (Fig. 13c), suggesting that strong intermolecular interactions enhance the stabilization of the radical cation.

XRD analyses showed that **11(OTf)** has a non-planar structure with three intermolecular π-stacking modes: head-to-head, head-to-tail and tail-to-tail interactions. The intermolecular distance is less than the C–C van der Waals radii (3.4 Å) (Fig. 13b), confirming that **11(OTf)** achieves electrostatically enhanced intermolecular covalent bonding interactions. DFT calculations on the **11(OTf)** dimers further demonstrate that these three tight π-stacking interactions enable intermolecular spin–spin coupling. Noticeably, a significant electrical conductivity of 1.31×10^{-2} S cm^{-1} was achieved based on the single-crystal **11(OTf)**.

Notably, in 2019, Chi and colleagues disclosed the successful synthesis of higher order O-doped quinoidal nonacene (**12.1**) and decacene (**12.3**) incorporating 1,4-benzoquinodimethane (*p*-BQDM) or 2,6-naphthoquinodimethane (*p*-NQDM) units, marked a significant advancement (Fig. 14).[38] Compound **12.1** exhibits a closed-shell structure and high ambient stability, while **12.3** possessing a moderate diradical character ($y_0 = 25.0\%$), is more reactive. To stabilize the reactive zigzag edges and enhance solubility, sterically bulky substituents such as mesityl (Mes) groups were strategically introduced onto the zigzag edges of the conjugated backbone. A "center-to-outer-edge" Friedel–Crafts (FC) cyclization tactic was employed for the synthesis of O-doped nonacene **12.1**. Initially, the **12.4** was reduced by LiAlH$_4$ to give the corresponding diol, which subsequently underwent FC cyclization in the presence of BF$_3$·Et$_2$O to give the key dihydro precursor **12.5**. Finally, oxidative dehydrogenation of **12.5** with DDQ furnished the O-doped nonacene **12.1** in 82% yield. For the construction of longer analogue **12.3**, an "outer-edge-to-center" strategy was utilized to give the key dihydro intermediate **12.7**. However, oxidative dehydrogenation of **12.7** resulted in the formation of an insoluble precipitate, which was attributed to the formation of a charge-transfer complex between excess DDQ and **12.2**. Interestingly, treatment of this precipitate with trifluoroacetic acid (TFA) generated radical species, were subsequently reduction with SnCl$_2$ successfully affording the doubly trifluoroacetyl substituted compound **12.3** in 8% yield.

XRD analysis revealed that both **12.1** and **12.3** possess nearly planar backbone, with the mesityl groups oriented almost perpendicular to the skeleton (Fig. 14c). The central *p*-BQDM unit in **12.1** exhibits a typical quinoidal structure, while the *p*-NQDM of **12.3** displays a reduced quinoidal character, as evidenced by the bond length analysis. Spin-unrestricted DFT calculations, nuclear independent chemical shift (NICS)
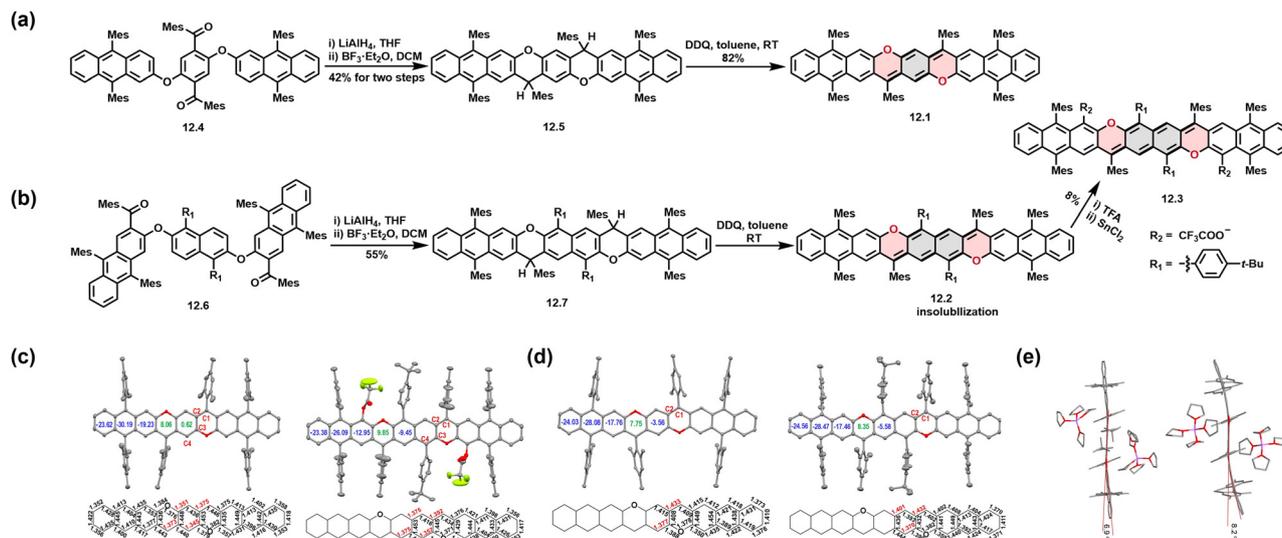
14194 | *J. Mater. Chem. C*, 2025, **13**, 14187–14201

This journal is © The Royal Society of Chemistry 2025

Fig. 14 Synthetic routes of **12.1** (a) and **12.3** (b). X-ray crystallographic structures, selected bond lengths (in Å) and calculated NICS(1)$_{zz}$ values of (c) **12.1**, **12.3**, (d) **12.1**$^{2-}$, **12.3**$^{2-}$ Side view of the structures of (e) **12.1**$^{2-}$ (left), **12.3**$^{2-}$ (right). Reproduced from ref. 38. Copyright 2019 American Chemical Society.

calculations, anisotropy calculations of induced current density (ACID), variable-temperature NMR and absorption spectroscopy results confirmed the closed-shell nature of **12.1** and the apparently open-shell singlet diradical nature of **12.3**. Charged species were also prepared to further investigate the ground states and electronic properties. **12.1**$^{2+}$ and **12.3**$^{2+}$ have a centrosymmetric structure, with the corresponding counter ions located above and below the conjugated backbone (Fig. 14d and e). The bending angles between the outer anthracene unit and the central quinone unit are 8.2° for **12.1**$^{2+}$ and 6.9° for **12.3**$^{2+}$. The dication (**12.1**$^{2+}$) and dianion (**12.1**$^{2-}$) of **12.1** exhibit open-shell biradical character, whereas both the **12.3**$^{2+}$ and **12.3**$^{2-}$ display closed-shell electronic configurations. This difference is attributed to the larger intramolecular Coulomb repulsion present in the charged states of **12.1** compared to those

of **12.3**. Additionally, the **12.1**$^{2+}$ and **12.3**$^{2+}$ can be regarded as the isoelectronic structures of the all-carbon nonacene and decacene, respectively. Notably, unlike the nonacene and decacene counterparts, these positively charged species exhibit significantly enhanced stability, owing to effective charge delocalization and reduced chemical reactivity.

In 2021, the Chi's group further advanced the design of stable higher-order O-doped acenes by introducing indeno fusion at the zigzag edges *via* Scholl-type oxidative cyclodehydrogenation. This approach led to the successful synthesis of tetraindeno-fused O-doped quinoidal nonacene (**13.1**).[39] As shown in Fig. 15, compound **13.2** underwent FeCl$_3$-mediated oxidative cyclodehydrogenation reaction, leading to the formation of the key intermediate **13.3**, which contains two rubicene moieties. Following a synthetic sequence similar to that used
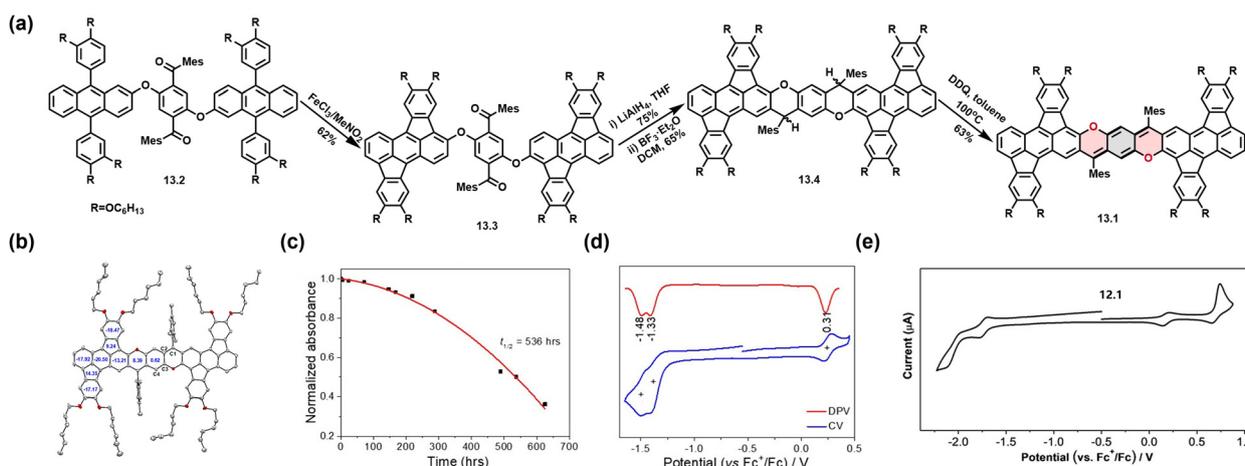
Fig. 15 (a) Synthetic routes to **13.1**. (b) X-ray crystallographic structures of **13.1**. (c) Plots of the optical density of **13.1** at 694 nm in DCM over the time. (d) Cyclic voltammogram and differential pulse voltammogram of **13.1** in DCM. (e) Cyclic voltammogram of **12.1** in DCM. Reproduced from ref. 39. Copyright 2021 American Chemical Society.

This journal is © The Royal Society of Chemistry 2025

J. Mater. Chem. C, 2025, **13**, 14187–14201 | **14195**

for compound **12.1**, including reduction, intramolecular FC alkylation, and oxidative dehydrogenation, the final tetraindeno-fused O-doped nonacene **13.1** was obtained. In solid state, **13.1** exhibits a slightly twisted π-conjugated backbone, resulting from close π–π stacking interactions between rubicene units of adjacent **13.1** molecules. Additionally, pronounced bond length alternation in the central benzenoid ring, indicates a classical quinoidal structure, comparable to that observed in **12.1** (Fig. 15b). Furthermore, the presence of sharp ^{1}H NMR signals at elevated temperatures (up to 333 K) supports its closed shell electronic configuration, aligns with the results from the DFT calculations. Notably, **13.1** demonstrated excellent stability, with a half-life time ($t_{1/2}$) of 536 hours (Fig. 15c), significantly outperforming that of **12.1** ($t_{1/2}$ = 157 hours) under ambient conditions. In addition, the calculated HOMO and LUMO energy levels of **13.1** were found to be −5.10 eV and −3.66 eV, respectively, which are lower compared to those of **12.1** (Fig. 15e), reflecting enhanced electronic stabilization. These experimental and theoretical results highlight that the fusion of indeno groups onto the zigzag edges not only enhances kinetic stability but also substantially alters the electronic properties of O-doped acenes.

In 2019, Zeng et al. developed an efficient one-pot cross condensation strategy for constructing quinoidal pentacene and nonacene derivatives featuring zigzag oxygen insertions (Fig. 16).[40] This method involves acid-promoted cross condensation between commercially available compounds **14.4** and **14.3**, providing a scalable and practical approach suitable for large-scale production. The carbon atom of carbonyl group in **14.4** was first protonated by a strong acid to generate a highly electrophilic hydroxymethyl intermediate, which subsequently undergoes FC reaction with **14.3**. Finally, ring closure is further facilitated by acid or heating, resulting in the formation of a six-membered pyranyl ring. The O-doped quinoidal pentacene (**14.1**) and nonacene **14.2**, each bearing two hydroxyl groups at the aromatic termini, were obtained in 54% and in 37% yields, respectively. Subsequent methylation of the hydroxyl groups afforded the corresponding methoxy-functionalized O-doped quinoidal pentacene (**14.1-Me**) and nonacene (**14.2-Me**)

in high yields exceeding 80%. Notably, both methylated compounds **14.1-Me** and **14.2-Me** exhibit excellent stability in solutions at ambient conditions for several months.

X-ray crystallographic analysis reveal that **14.1-Me** and **14.2-Me** possess nearly planar backbones, with two or four oxygen atoms clearly positioned at the zigzag peripheries. The bond lengths of the bridged cyclohexa-1,4-diene rings range from 1.35–1.39 Å (highlighted in blue, Fig. 16b), suggesting their quinoidal nature. Furthermore, the C–O bond lengths (labelled in red) in **14.1-Me** and **14.2-Me** are shorter than those typical C–O single bonds, indicating significant delocalization of the lone pairs of oxygen into the π-system. Interestingly, the NICS calculations revealed a weak anti-aromatic character within these O-doping six-membered rings. The electronic properties of these O-doped acenes are reflected in their UV-vis absorption spectra. For instance, compounds **14.2/14.2-Me**, which feature four O-doped hexagons, exhibit a redshift of approximately 160 nm and nearly double the molar absorption coefficient (ε) compared to **14.1/14.1-Me**, which contain only two O-doped hexagons (Fig. 16c). The optical energy gaps were estimated to be 2.14 eV for **14.1-Me** and 1.48 eV for **14.2-Me**, indicating that the energy gap narrows with longitudinal extension of the O-doped acenes. It is noteworthy that **14.2/14.2-Me** exhibit low-energy absorption bands spanning 770 nm to 850 nm, highlighting that the electronic structure of O-doped acenes can be effectively modulated by increasing the number of O-containing rings and quinoidal segments. The electrochemical energy gaps of **14.1-Me** and **14.2-Me** were measured to be 1.98 eV and 1.46 eV, respectively, aligning well with their optical energy gaps and showing excellent agreement with DFT-calculated values. Moreover, the hole mobility of **14.1-Me** in thin film FETs was measured to be 4.06 × 10^{-3} cm^2 V^{-1} s^{-1}, surpassing those of sulfur-doped quinoidal pentacene analogues under ambient conditions. This study provides valuable insights into the relationship between how O-doping patterns and molecular extension modulate the structural and optoelectronic properties of quinoidal O-doped PAHs.
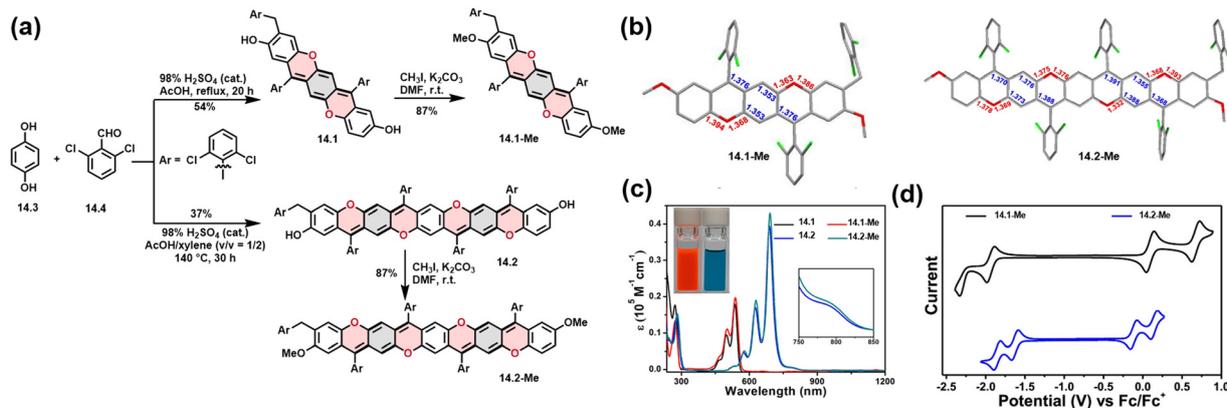

Fig. 16 (a) Synthetic routes to **14.1/14.1-Me** and **14.2/14.2-Me**. (b) X-ray crystallographic structures of **14.1-Me** and **14.2-Me**, selected bond lengths in Å. (c) UV–vis–NIR absorption spectra of **14.1/14.1-Me** and **14.2/14.2-Me**. (d) Cyclic voltammetry measurements of **14.1-Me** and **14.2-Me**. Reproduced from ref. 40. Copyright 2019 American Chemical Society.

14196 | *J. Mater. Chem. C*, 2025, **13**, 14187–14201

This journal is © The Royal Society of Chemistry 2025

3. Furanyl-bridged fused benzofuran

Furan is a key structural motif commonly found in natural products and is known for its diverse biological activities, including anticarcinogenic, antiviral, and antioxidant properties.[41] In addition to the previously mentioned O-doped PAHs with six-membered pyrano and pyranyl rings, the incorporation of furan units into aromatic skeletons represents an appealing strategy for constructing oxygen-containing PAHs.[42] Compared to thiophene analogues, furan derivatives typically exhibit higher solubility and better processability. Furan-embedded PAHs are expected to exhibit relatively high HOMO energy levels, rendering them promising candidates for applications in organic electronics. Various representative benzofuran derivatives (Fig. 17) have been successfully synthesized, and their structural, electronic, and optoelectronic properties have been thoroughly characterized to date.

Tsubaki and colleagues employed a bottom-up synthetic approach to construct a series of oligonaphthofurans consisting of alternating naphthalene and furan units.[43] The largest synthesized structure was 15.1, which consists of alternating seven furan and eight naphthalene units arranged in a distinctive fan-shaped structure (Fig. 18).[44] The synthesis of target compound 15.1 involves a self-coupling reaction with CuCl₂ from the starting material 15.2, followed by an alkylation

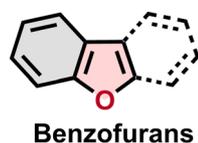reaction with *n*-BuBr to produce 15.3. Compound 15.3 was subsequently converted to 15.4 through formylation, a Wittig reaction, and hydrogenation. Lithiation of 15.4, followed by the introduction of dimethoxyborane and oxidation, gave the key hydroxyl-functionalized intermediate 15.5, which enabled further extension of the oligonaphthofuran backbone. DFT calculations indicated that not only 15.1 but also its shorter analogues (2-mer, 3-mer, 4-mer and 6-mer) adopt fan-shaped geometries, driven by steric repulsion between hydrogen atoms on adjacent naphthalene units (Fig. 18b). These molecules exhibit an alternating valley-like conformation, which disrupts planarity while preserving π-conjugation across the central backbone. Furthermore, as the oligomer length increases from 4-mer to 8-mer, the HOMO and LUMO become increasingly localized toward the molecular core (Fig. 18c). Notably, greater coefficients for the inner benzene ring are observed for a single naphthalene unit. As a result, the inner benzene rings and furan rings provide most of the π-conjugation on the molecule, which is consistent with the observed constant redshifts in absorption and the decrease in molar absorption coefficient of the fan-shaped oligonaphthofurans as the number of aromatic rings increases. These electronic features underline the potential of such π-architectures in tunable optoelectronic applications.

In 2020, Kato's group reported the synthesis of difluoreno-[4,3-*b*:3′,4′-*d*]furan (16.1) (Fig. 19),[45] a molecule incorporating Tschitschibabin's hydrocarbon motif to access open-shell singlet diradical character.[46] The synthesis of 16.1 was accomplished through a five-step sequence starting from commercially available dibenzofuran (16.2). First, direct lithiation of 16.2 followed by treatment with I₂ yielded the iodinated intermediate 16.3.

Benzofurans

Fig. 17 Representative structure of benzofurans and its derivatives.
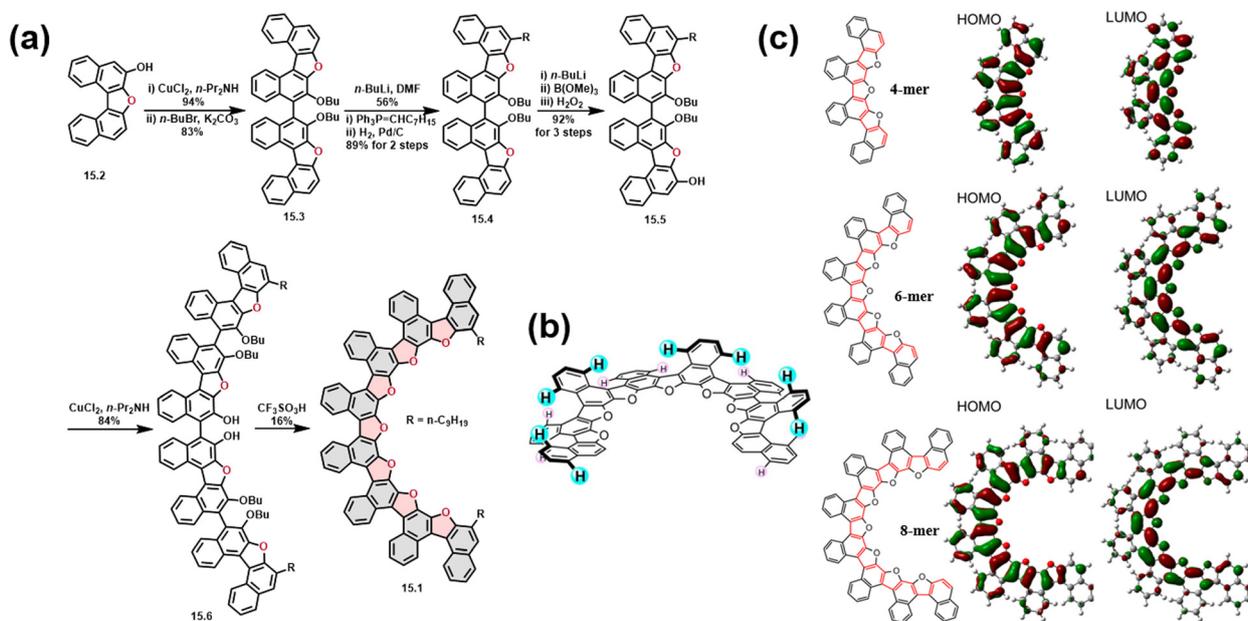
Fig. 18 (a) Synthetic routes to 15.1. (b) Optimized structures of 15.1 by DFT calculations for the alternating mountain–valley folds conformation. (c) Optimized structures of 4mer, 6mer and 8mer with their HOMOs and LUMOs. DFT calculations were at the B3LYP/6-31G(d,p) level. Reproduced from ref. 44. Copyright 2014 American Chemical Society.
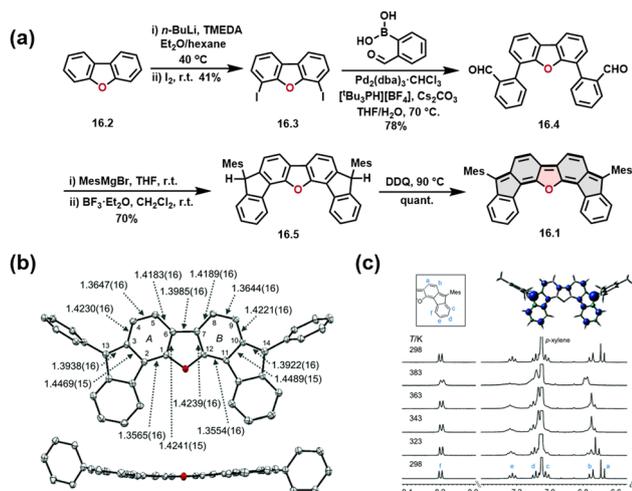
This journal is © The Royal Society of Chemistry 2025

J. Mater. Chem. C, 2025, **13**, 14187–14201 | **14197**

Fig. 19 (a) Synthetic routes to **16.1**. (b) Crystal structure of **16.1**. Bond lengths are given in Å. (c) Temperature-dependent ¹H NMR spectra of **16.1** and spin-density distribution of the open-shell triplet state of **16.1** (UB3LYP/6-311G(d)). Reproduced from ref. 45. Copyright 2020 The Royal Society of Chemistry.

Compound **16.3** then underwent a Suzuki–Miyaura coupling with 2-formylphenylboronic acid to give the aldehyde derivative **16.4**. Subsequent nucleophilic addition with mesitymagnesium bromide and followed by an intramolecular FC alkylation produced the dihrdro compound **16.5** in 70% yield over two

steps. Finally, oxidative dehydrogenation of **16.5** with DDQ gave the product **16.1** in nearly quantitative yield. X-ray crystallographic analysis revealed a slightly bent π-backbone, with deviations from ideal coplanarity ranging from 0.009 Å to 0.236 Å. The flanking 2,4,6-trimethylphenyl substituents adopted large dihedral angles of 73° and 78° relative to the central core. Bond length alternation was clearly observed in rings **A** and **B**, indicating that compound **16.1** exhibits a typical quinoidal structure with substantial diradical contribution to the ground state. (Fig. 19b). In addition, the broadening of the ¹H NMR signals with increasing temperature suggests an open-shell singlet diradical character of **16.1** (Fig. 19c). These experimental observations were corroborated by spectroscopic analyses and DFT calculations, confirming its open-shell singlet ground state.

In 2023, Zeng and co-workers reported the synthesis of stable tetrafuranylperylene (**17.1**) and octafuranylquaterrylene (**17.2**) derivatives with *fjord* edge topologies by incorporating furan units (Fig. 20).[47] The synthesis commenced with tetra-alkynylated perylene (**17.3**), which was prepared *via* Sonogashira cross-coupling of an *ortho*-tetrabrominated perylene precursor with 1-hexyne.[48] Treatment of compound **17.3** with I_2 under microwave radiation, in the presence of $NaHCO_3$/dichloroethane at elevated temperature, afforded compound **17.4** in 53% yield. Single crystal XRD analysis confirmed that **17.4** features two oxygen-embedded *fjord*-edged structure. Subsequent cyanation of **17.4** yielded tetrafuranylperylene
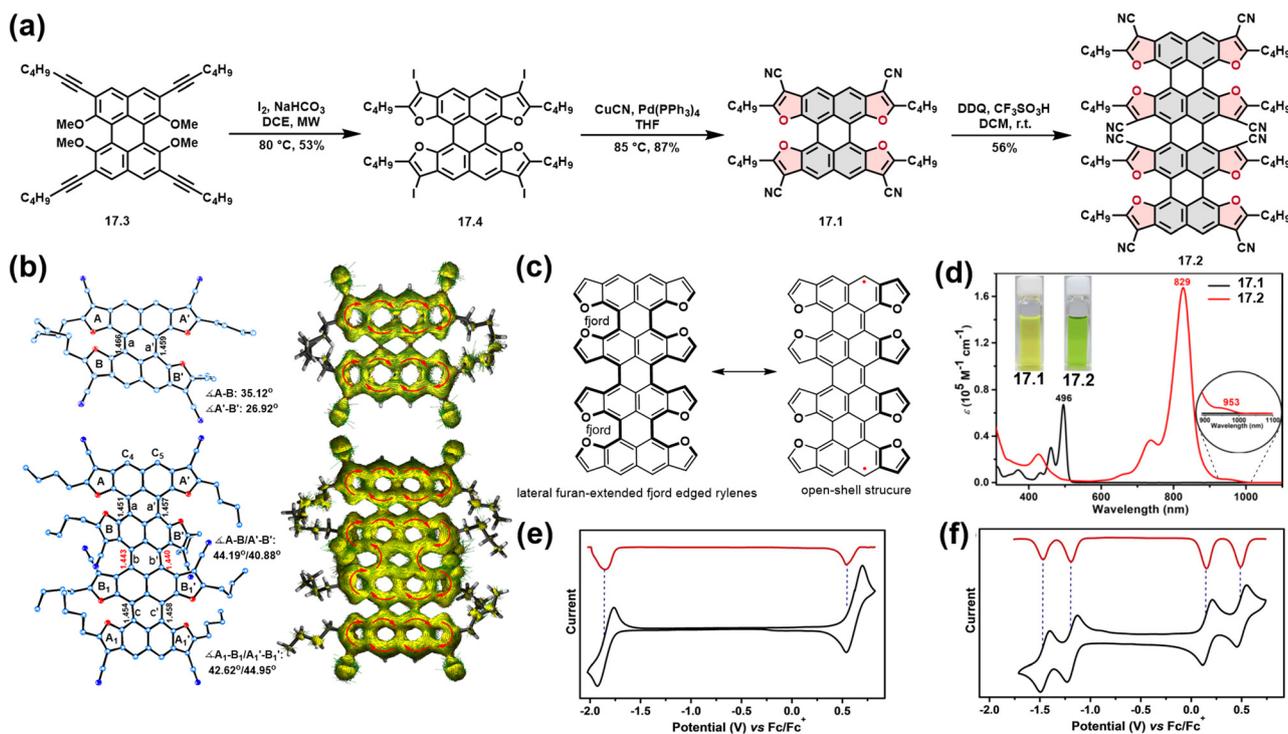
Fig. 20 (a) Synthetic routes to **17.1** and **17.2**. (b) X-ray single crystal structures and calculated ACID plots (isovalue = 0.01) of **17.1** and **17.2**. (c) Lateral furan-extended *fjord* edged rylenes and its open-shell structure. (d) UV/Vis-NIR absorption spectra of **17.1** and **17.2**. (e) Cyclic voltammograms (black) and differential pulse voltammogram (red) of **17.1**. (f) Cyclic voltammograms (black) and differential pulse voltammogram (red) of **17.2**. Reproduced from ref. 47. Copyright 2022 Wiley-VCH Gmbh.

14198 | J. Mater. Chem. C, 2025, **13**, 14187–14201

This journal is © The Royal Society of Chemistry 2025

17.1, which was further subjected to a homocoupling reaction, producing the octacyano-substituted octafuranylquaterrylene **17.2** (Fig. 20a). The structures of both **17.1** and **17.2** were unambiguously verified by XRD, revealing their distinct *fjord*-edged π-conjugated backbones (Fig. 20b). Both Compounds **17.1** and **17.2** show excellent stability under ambient conditions, which is attributed to strategic O-doping at specific *fjord*-edge sites and the incorporation of electron-withdrawing cyano groups on the reactive zigzag peripheries.

A comprehensive suite of experimental and computational investigations, including variable-temperature NMR, electron paramagnetic resonance (EPR), superconducting quantum interference device (SQUID) measurements and ACID calculations, demonstrated a transition from a closed-shell nature in **17.1** to an open-shell diradicaloid character in **17.2** (Fig. 20c). In addition, compared to **17.1**, the molecule **17.2** shows a significant redshift at about 333 nm (Fig. 20d), a strong absorption band at about 829 nm, a weak electronic absorption shoulder at about 953 nm, and a significant decrease in the HOMO–LUMO band gap. (about 1.08 eV, Fig. 20e and f). These findings accurately illustrate that the electronic properties of **17.1** and **17.2** are strongly related to the *fjord* edge length. This is because the introduction of the furan ring leads to a greater degree of exocyclic conjugation of π electrons throughout the conjugated backbone, while simultaneously lengthening the *fjord* edge, causing the molecule to progressively exhibit a diradicaloid nature. This study provides valuable insight into the relationship between the edge topology, electronic structure and the optoelectronic properties in O-doped rylene-type PAHs. It highlights the effectiveness of furan-based edge engineering as an effective strategy to modulate molecular curvature, conjugation, and electronic functionality in π-conjugated systems.

4. Summary and outlook

O-Doped polycyclic aromatic hydrocarbons (PAHs) have emerged as a compelling class of functional materials, where the strategic incorporation of oxygen atoms into π-conjugated frameworks enables precise modulation of their optoelectronic, structural, and magnetic properties. Stemming not only from the small atomic radius, high electronegativity, and π-delocalization ability of oxygen, but also from the strategic modulation of ring fusion patterns and heteroatom positioning within the PAH frameworks, recent advances have demonstrated that O-doping—through pyranopyranyl, furanyl, or other oxygen-embedded moieties—confers several key advantages: (i) bandgap engineering, where oxygen's high electronegativity and π-delocalization ability reduce energy gaps while maintaining tunable charge transport characteristics (*e.g.*, p-type to ambipolar behavior); (ii) enhanced stability and three-dimensionality, driven by rigid heterocyclic fusion and unique solid-state packing motifs; (iii) emergence of open-shell diradical character in quinoidal systems, which might facilitate spin manipulation for spintronic applications; and (iv) distinct photophysical properties, such as redshifted absorption/emission and tailored exciton dynamics, advantageous for optoelectronic devices.

Despite this promising progress, it should be noted that challenges remain to fully harness the potential of O-doped PAHs. For instance, compared to other heteroatom-doped systems, current synthetic methods for large, structurally well-defined O-doped PAHs (*e.g.*, extended O-embedded nano-graphenes) are rather limited, especially for those with high preparation efficiency. Therefore, it is highly demanded to develop new O-embedded motifs (such as O-contained seven-membered rings) with capability of facile structural expansion and robust strategies for atomically precise, scalable synthesis of extended O-doped PAHs. The incorporation of oxygen atoms along with other heteroatoms into a single aromatic framework may also provide alternative pathways for designing novel PAHs with precisely tailored properties. However, a deeper understanding of the synergistic effects in such co-doped systems is needed to better guide the structural design of these heteroatom-modified PAHs. By addressing these challenges, it is believed that O-doped PAHs could transcend their current niche and potentially offer a versatile material platform for the next-generation of organic electronics, spintronics, and beyond.

Author contributions

The manuscript was written through contributions of all authors. All authors have given approval to the final version of the manuscript.

Conflicts of interest

There are no conflicts to declare.

Data availability

No primary research results, software or code have been included, and no new data were generated or analysed as part of this review.

Acknowledgements

References

1 K. S. Novoselov, A. K. Geim, S. V. Morozov, D. Jiang, Y. Zhang, S. V. Dubonos, I. V. Grigorieva and A. A. Firsov, *Science*, 2004, **306**, 666–669.

2 (*a*) A. Narita, X. Y. Wang, X. Feng and K. Müllen, *Chem. Soc. Rev.*, 2015, **44**, 6616–6643; (*b*) X. Y. Wang, X. Yao and K. Müllen, *Sci. China: Chem.*, 2019, **62**, 1099–1144;

This journal is © The Royal Society of Chemistry 2025

J. Mater. Chem. C, 2025, **13**, 14187–14201 | **14199**

(c) B. Chan and A. Karton, *Phys. Chem. Chem. Phys.*, 2021, **23**, 17713–17723.

3 (a) L. Zhang, Y. Cao, N. S. Colella, Y. Liang, J. L. Bredas, K. N. Houk and A. L. Briseno, *Acc. Chem. Res.*, 2015, **48**, 500–509; (b) Q. Li, Y. Zhang, Z. Xie, Y. Zhen, W. Hu and H. Dong, *J. Mater. Chem. C*, 2022, **10**, 2411–2430; (c) Y. Gu, Z. Qiu and K. Müllen, *J. Am. Chem. Soc.*, 2022, **144**, 11499–11524; (d) K. Yang, Z. Li, Y. Huang and Z. Zeng, *Acc. Chem. Res.*, 2024, **57**, 763–775.

4 Y. Wang, B. Liu, C. W. Koh, X. Zhou, H. Sun, J. Yu and X. Guo, *Adv. Energy Mater.*, 2019, **9**, 1803976.

5 (a) W. Li, C. Z. Du, X. Y. Chen, L. Fu, R. R. Gao, Z. F. Yao and X. Y. Wang, *Angew. Chem., Int. Ed.*, 2022, **134**, e202201464; (b) N. Zhang, L. Yang, W. Li, J. Zhu, K. Chi, D. Chang and Y. Liu, *J. Am. Chem. Soc.*, 2022, **144**, 21521–21529; (c) R. Zhang, W. Li, Y. Gu, T. Wang, J. Zhang, K. Chi and Y. Zhao, *Angew. Chem., Int. Ed.*, 2025, e202501686.

6 (a) X. Wang, Y. Zhang, H. Dai, G. Li, M. Liu, G. Meng and L. Duan, *Angew. Chem., Int. Ed.*, 2022, **134**, e202206916; (b) G. Li, K. Xu, J. Zheng, X. Fang, Y. F. Yang, W. Lou and Y. B. She, *Nat. Commun.*, 2023, **14**, 7089; (c) Y. Wu, X. Liu, J. Liu, G. Yang, Y. Deng, Z. Bin and J. You, *J. Am. Chem. Soc.*, 2024, **146**, 15977–15985.

7 (a) K. Cai, J. Xie and D. Zhao, *J. Am. Chem. Soc.*, 2014, **136**, 28–31; (b) N. Baig, S. Shetty, R. Bargakshatriya, S. K. Pramanik and B. Alameddine, *ACS Omega*, 2024, **9**, 36732–36740.

8 (a) M. Stepien, E. Gonka, M. Żyła and N. Sprutta, *Chem. Rev.*, 2017, **117**, 3479–3716; (b) A. Borissov, Y. K. Maurya, L. Moshniaha, W. S. Wong, M. Żyła-Karwowska and M. Stepien, *Chem. Rev.*, 2021, **122**, 565–788.

9 J. Zhu, R. Zhang, D. An, Y. Gu, X. Lu and Y. Liu, *Acc. Mater. Res.*, 2025, **6**, 523–537.

10 X. Deng, X. Yu, J. Xiao and Q. Zhang, *Aggregate*, 2021, **2**, e35.

11 (a) S. K. Mellerup and S. Wang, *Trends Chem.*, 2019, **1**, 77–89; (b) C. Chen, C. Z. Du and X. Y. Wang, *Adv. Sci.*, 2022, **9**, 2200707; (c) J. Guo, K. Zhang, Y. Wang, H. Wei, W. Xiao, K. Yang and Z. Zeng, *Chem. Sci.*, 2023, **14**, 4158–4165; (d) T. Huang, Z. Ding, H. Liu, P. A. Chen, L. Zhao, Y. Hu and Z. Zeng, *Chin. Chem. Lett.*, 2024, **35**, 109117.

12 (a) Z. Li, Y. Tang, J. Guo, J. Zhang, M. Deng, W. Xiao and Z. Zeng, *Chem*, 2023, **9**, 1281–1294; (b) Z. Li, Y. Bu, S. Xie, Y. Ni, K. Yang and Z. Zeng, *Chem. Mater.*, 2024, **36**, 3058–3080; (c) X. L. Chen, S. Q. Yu, J. Q. Liang, X. Huang and H. Y. Gong, *Org. Chem. Front.*, 2025, **12**, 1340–1354.

13 R. Szűcs, P. A. Bouit, L. Nyulászi and M. Hissler, *ChemPhysChem*, 2017, **18**, 2618–2630.

14 (a) Y. Li, A. Concellón, C. J. Lin, N. A. Romero, S. Lin and T. M. Swager, *Chem. Sci.*, 2020, **11**, 4695–4701; (b) O. Matuszewska, T. Battisti, R. R. Ferreira, N. Biot, N. Demitri and D. Bonifazi, *Chem. – Eur. J.*, 2023, **29**, e202203115; (c) Z. Zhou, K. Yang, L. He, W. Wang, W. Lai, Y. Yang and Z. Zeng, *J. Am. Chem. Soc.*, 2024, **146**, 6763–6772; (d) L. Zhao, H. Liu, W. Li, Y. Yang, X. He, Z. Zhang, Y. Zhao, Y. Yao, L. Sun, K. Yang and Z. Zeng, *Angew. Chem., Int. Ed.*, 2025, **64**, e202507603; (e) T. Huang,

K. Yang, W. Hu, L. Feng, Z. Wu, H. Chen, J. Wang and Z. Zeng, *Chem*, 2025, **11**, 102621.

15 (a) A. Jha and P. J. J. Huang, *J. Heterocycl. Chem.*, 2009, **46**, 1098–1106; (b) O. Anamimoghadam, M. D. Symes, D. L. Long, S. Sproules, L. Cronin and G. Bucher, *J. Am. Chem. Soc.*, 2015, **137**, 14944–14951; (c) D. Stassen, N. Demitri and D. Bonifazi, *Angew. Chem., Int. Ed.*, 2016, **128**, 6051–6055; (d) I. Papadakis, Z. Bouza, A. Stathis, I. Orfanos, S. Couris, T. Miletic and D. Bonifazi, *J. Phys. Chem. A*, 2018, **122**, 5142–5152; (e) L. Đorđević, C. Valentini, N. Demitri, C. Mézière, M. Allain, M. Sallé and D. Bonifazi, *Angew. Chem., Int. Ed.*, 2020, **132**, 4135–4143; (f) Y. Han, W. C. Guo, X. S. Du and C. F. Chen, *Chem. Commun.*, 2024, **60**, 5719–5722.

16 Y. Wang, S. Qiu, S. Xie, L. Zhou, Y. Hong, J. Chang and Z. Zeng, *J. Am. Chem. Soc.*, 2019, **141**, 2169–2176.

17 D. Wu, W. Pisula, M. C. Haberecht, X. Feng and K. Müllen, *Org. Lett.*, 2009, **11**, 5686–5689.

18 V. Balasubramaniyan, *Chem. Rev.*, 2004, **104**, 2735–2754.

19 (a) R. Pummerer, E. Prell and A. Rieche, *Ber. Dtsch. Chem. Ges.*, 1926, **59**, 2159–2161; (b) T. Asari, N. Kobayashi, T. Naito and T. B. Inabe, *Bull. Chem. Soc. Jpn.*, 2001, **74**, 53–58; (c) T. Kamei, M. Uryu and T. Shimada, *Org. Lett.*, 2017, **19**, 2714–2717.

20 (a) M. Hjorth, N. Thorup, P. Frederiksen and K. Bechgaard, *Acta Chem. Scand.*, 1994, **48**, 139–143; (b) T. Asari, T. Naito, T. Inabe, M. Matsuda and H. Tajima, *Chem. Lett.*, 2004, **33**, 128–129.

21 Y. Chen, Z. Q. Li, Y. Q. Deng, B. Y. Yu, W. L. Pan and H. C. Song, *Chem. Pharm. Bull.*, 2019, **67**, 690–692.

22 S. Fujii and T. Enoki, *Acc. Chem. Res.*, 2013, **46**, 2595–2604.

23 N. Kobayashi, M. Sasaki and K. Nomoto, *Chem. Mater.*, 2009, **21**, 552–556.

24 L. Wang, G. Duan, Y. Ji and H. Zhang, *J. Phys. Chem. C*, 2012, **116**, 22679–22686.

25 N. Lv, M. Xie, W. Gu, H. Ruan, S. Qiu, C. Zhou and Z. Cui, *Org. Lett.*, 2013, **15**, 2382–2385.

26 N. Xu, Y. Li, R. Wu, R. Zhu, J. Zhang, S. M. Zakeeruddin, H. Li, Z. S. Li, M. Grätzel and P. Wang, *Chem. – Eur. J.*, 2019, **25**, 945–948.

27 D. Stassen, N. Demitri and D. Bonifazi, *Angew. Chem., Int. Ed.*, 2016, **128**, 6051–6055.

28 A. Berezin, N. Biot, T. Battisti and D. Bonifazi, *Angew. Chem., Int. Ed.*, 2018, **57**, 8942–8946.

29 T. Miletić, A. Fermi, I. Orfanos, A. Avramopoulos, F. De Leo, N. Demitri, G. Bergamini, P. Ceroni, M. G. Papadopoulos, S. Couris and D. Bonifazi, *Chem. – Eur. J.*, 2017, **23**, 2363–2378.

30 (a) A. Sciutto, A. Fermi, A. Folli, T. Battisti, J. M. Beames, D. M. Murphy and D. Bonifazi, *Chem. – Eur. J.*, 2018, **24**, 4382–4389; (b) A. Sciutto, A. Berezin, M. L. Cicero, T. Miletić, A. Stopin and D. Bonifazi, *J. Org. Chem.*, 2018, **83**, 13787–13798.

31 Š. Vyskočil, L. Meca, I. Tišlerová, I. Císařová, M. Polášek, S. R. Harutyunyan, Y. N. Belokon, R. M. J. Stead, L. Farrugia, S. C. Lockhart, W. L. Mitchell and P. Kočovsky, *Chem. – Eur. J.*, 2002, **8**, 4633–4648.

14200 | *J. Mater. Chem. C*, 2025, **13**, 14187–14201

This journal is © The Royal Society of Chemistry 2025

32 K. Zhang, J. Guo, H. Liu, X. Wang, Y. Yao, K. Yang and Z. Zeng, *Chem. Commun.*, 2023, **59**, 4947–4950.

33 (*a*) Z. Zeng, X. Shi, C. Chi, J. T. L. Navarrete, J. Casado and J. Wu, *Chem. Soc. Rev.*, 2015, **44**, 6578–6596; (*b*) Q. Jiang, H. Wei, X. Hou and C. Chi, *Angew. Chem., Int. Ed.*, 2023, **62**, e202306938.

34 W. Zeng and J. Wu, *Chem*, 2021, **7**, 358–386.

35 (*a*) X. Shi, W. Kueh, B. Zheng, K. W. Huang and C. Chi, *Angew. Chem., Int. Ed.*, 2015, **54**, 14412–14416; (*b*) S. Dong, T. S. Herng, T. Y. Gopalakrishna, H. Phan, Z. L. Lim, P. Hu, R. D. Webster, J. Ding and C. Chi, *Angew. Chem., Int. Ed.*, 2016, **55**, 9316–9320; (*c*) Y. Chen, H. Kueh, T. Y. Gopalakrishna, S. Dong, Y. Han and C. Chi, *Org. Lett.*, 2019, **21**, 3127–3130.

36 W. L. Kalb, A. F. Stassen, B. Batlogg, U. Berens, B. Schmidhalter, F. Bienewald, A. Hafner and T. Wagner, *J. Appl. Phys.*, 2009, **105**, 043705.

37 C. M. Wehrmann, R. T. Charlton and M. S. Chen, *J. Am. Chem. Soc.*, 2019, **141**, 3240–3248.

38 S. Dong, T. Y. Gopalakrishna, Y. Han, H. Phan, T. Tao, Y. Ni, G. Liu and C. Chi, *J. Am. Chem. Soc.*, 2019, **141**, 62–66.

39 J. J. C. Lee, S. Dong, A. Ong, Y. Han, J. Wu and C. Chi, *Org. Lett.*, 2021, **23**, 3027–3031.

40 Y. Wang, S. Qiu, S. Xie, L. Zhou, Y. Hong, J. Chang, J. Wu and Z. Zeng, *J. Am. Chem. Soc.*, 2019, **141**, 2169–2176.

41 (*a*) S. Zacchino, G. Rodriguez, G. Pezzenati, G. Orellana, R. Enriz and S. M. Gonzalez, *J. Nat. Prod.*, 1997, **60**, 659–662; (*b*) C. Cow, C. Leung and J. L. Charlton, *Can. J. Chem.*, 2000, **78**, 553–561; (*c*) E. Navarro, S. J. Alonso, J. Trujillo, E. Jorge and C. Perez, *J. Nat. Prod.*, 2001, **64**, 134–135; (*d*) D. H. S. Silva, F. C. Pereira, M. V. B. Zanoni and M. Yoshida, *Phytochemistry*, 2001, **57**, 437–442.

42 (*a*) S. Wang, B. Lv, Q. Cui, X. Ma, X. Ba and J. Xiao, *Chem. – Eur. J.*, 2015, **21**, 14791–14796; (*b*) C. Mitsui, J. Soeda, K. Miwa, K. Shoyama, Y. Ota, H. Tsuji, J. Takeya and E. Nakamura, *Bull. Chem. Soc. Jpn.*, 2015, **88**, 776–783; (*c*) C. Mitsui, Y. Tanaka, S. Tanaka, M. Yamagishi, K. Nakahara, M. Yano, H. Sato, A. Yamano, H. Matsui, J. Takeya and T. Okamoto, *RSC Adv.*, 2016, **6**, 28966–28969; (*d*) T. Miletić, A. Fermi, I. Orfanos, A. Avramopoulos, F. D. Leo, N. Demitri, G. Bergamini, P. Ceroni, M. G. Papadopoulos, S. Couris and D. Bonifazi, *Chem. – Eur. J.*, 2017, **23**, 2363–2378; (*e*) N. N. Karaush, G. V. Baryshnikov, H. Ågren and B. F. Minaev, *New J. Chem.*, 2018, **42**, 11493–11505; (*f*) D. Chen, J. Li, W. Ma, B. Li, Y. Zhen, X. Zhu, W. Hu, H. Tsuji and E. Nakamura, *Asian J. Org. Chem.*, 2018, **7**, 2228–2232; (*g*) M. Feofanov, V. Akhmetov, R. Takayama and K. Amsharov, *Angew. Chem., Int. Ed.*, 2021, **60**, 5199–5203.

43 (*a*) K. Nakanishi, T. Sasamori, K. Kuramochi, N. Tokitoh, T. Kawabata and K. Tsubaki., *J. Org. Chem.*, 2014, **79**, 2625–2631; (*b*) T. Shouda, K. Nakanishi, N. Tokitoh, K. Kuramochi and K. Tsubaki, *J. Org. Chem.*, 2017, **82**, 7850–7855.

44 K. Nakanishi, D. Fukatsu, K. Takaishi, T. Tsuji, K. Uenaka, K. Kuramochi, T. Kawabata and K. Tsubaki, *J. Am. Chem. Soc.*, 2014, **136**, 7101–7109.

45 S. Mori, M. Akita, S. Suzuki, M. S. Asano, M. Murata, T. Akiyama, T. Matsumoto, C. Kitamura and S. Kato, *Chem. Commun.*, 2020, **56**, 5881–5884.

46 Z. Zeng, Y. M. Sung, N. Bao, D. Tan, R. Lee, J. L. Zafra, B. S. Lee, M. Ishida, J. Ding, J. T. L. Navarrete, Y. Li, W. Zeng, D. kim, K. Huang, R. D. Webster, J. Casado and J. Wu, *J. Am. Chem. Soc.*, 2012, **134**, 14513–14525.

47 T. Luo, Y. Wang, J. Hao, P. A. Chen, Y. Hu, B. Chen, J. Zhang, K. Yang and Z. Zeng, *Angew. Chem., Int. Ed.*, 2023, **135**, e202214653.

48 Y. Li, Y. Hong, J. Guo, X. Huang, H. Wei, J. Zhou, T. Qiu, J. Wu and Z. Zeng, *Org. Lett.*, 2017, **19**, 5094–5097.

This journal is © The Royal Society of Chemistry 2025

J. Mater. Chem. C, 2025, **13**, 14187–14201 | 14201